BNL-228880-2025-JAAM

Plasmon Dynamics Driven by Aggregation of Tris(2,2′-bipyridine)ruthenium(II)-Functionalized Gold Nanoparticles Probed by XANES and Transient Absorption Spectroscopy

P. Srivastava, A. Pattammattel

To be published in "The Journal of Physical Chemistry C"

July 2025

Photon Sciences

Brookhaven National Laboratory

U.S. Department of Energy

USDOE Office of Science (SC), Basic Energy Sciences (BES). Scientific User Facilities (SUF)

DISCLAIMER

Plasmon Dynamics Driven by Aggregation of Tris(2,2'-bipyridine)ruthenium(II) - Functionalized Gold Nanoparticles Probed by XANES and Transient Absorption Spectroscopy

Prasenjit Srivastava,[†] Natalie Warren,[†] Andes Willemsen,[†] Umar Yunusa,[†] Ajith Pattammattel,[‡] and Emily Sprague-Klein*,[†]

†*Department of Chemistry, Brown University, Providence, RI, 02912, United States*

‡*National Synchotron Light Source II, Brookhaven National Lab, Upton, NY, 11973, United States*

E-mail: emily_sprague-klein@brown.edu

September 4, 2025

Abstract

Energy conversion dynamics are critical for advancing next-generation photovoltaics, optoelectronics, and light-harvesting technologies. Noble metal plasmonic nanoparticles play a pivotal role as nanoscale electromagnetic confinement structures, driving photon-induced chemical reactions. In this study, we explore the effects of $[Ru(bpy)_3]^{2+}$ functionalization

and aggregation on citrate-capped gold nanoparticles (AuNPs) of 40 nm and 100 nm diameters, focusing on molecule-plasmon interactions and its influence on electronic and energy dissipation properties. X-ray absorption near-edge spectroscopy (XANES) reveals that $[Ru(bpy)_3]^{2+}$ functionalization induces controlled aggregation without altering the oxidation state of gold. A more pronounced white-line intensity is observed in 40 nm AuNPs, consistent with greater s–p–d hybridization and a higher density of surface states, likely influenced by both nanoparticle size and aggregation. Transient absorption (TA) spectroscopy highlights faster electron-phonon relaxation dynamics in aggregated 40 nm nanoparticles which is attributed to increased electron delocalization and more efficient coupling to the phonon bath. In contrast, 100 nm nanoparticles exhibit minimal changes due a lower degree of aggregation. Interestingly, we observe that enhanced electron–phonon coupling in aggregated nanoparticles coincides with a slowing of electron–electron scattering. These observations suggests a competitive interplay between the two relaxation pathways - where enhanced energy transfer to the lattice in aggregated systems can suppress electronic thermalization. These findings underscore the critical role of nanoparticle size, aggregation, and molecule-surface interactions in modulating plasmonic dynamics and excited-state lifetimes and further provide valuable insights for designing tailored plasmonic systems with transformative potential for sensing, catalysis, and energy conversion.

Introduction

The tailoring of nanomaterials for applications in optoelectronics[1,2], sensors[3,4], and light-energy conversion[5,6] represents one of the most dynamic areas of research in recent decades.[7–9] Noble metal nanoparticles, such as gold and silver, exhibit unique optical and electronic properties arising from their localized surface plasmon resonances (LSPRs), which are collective oscillation of conduction band electrons driven by incident light.[10–13] These resonances enable the confinement of light at the nanoscale level, enhancing optical phenomena such as

Raman scattering and fluorescence, and also enable efficient energy transfer processes.[14–16] The spectral characteristics of LSPR, including its intensity, position, and width, are strongly influenced by nanoparticle size, shape, surface chemistry, and aggregation state.[17–20] This tunability facilitates the design of systems with tailored properties for advanced technological applications.[20–23] The potential to exploit these properties for chemical selectivity, catalytic efficiency, and biological sensing has spurred extensive efforts to understand and control nanoparticle morphology.[8,24–26] However, many challenges remain in designing and characterizing plasmonic systems that achieve optimal coupling between nanoparticles and surface-bound molecules especially under conditions that promote aggregation.

Functionalizing metal nanoparticles with fluorophores or chromophores has emerged as a key strategy for developing biological sensors and optoelectronic devices.[27–30] Among these, *tris*(bipyridine)-ruthenium(II) ($[Ru(bpy)_3]^{2+}$) complexes are particularly promising due to their remarkable photophysical properties, including strong visible light absorption, long lived excited states, and efficient metal-to-ligand charge transfer (MLCT).[31–33] These complexes have been widely studied for their roles in solar energy conversion, photocatalysis, and photodynamic therapy.[34–37] While the intrinsic kinetics of these complexes are well-characterized, their integration with plasmonic nanoparticles introduces a unique interplay between molecular photophysics and nanoparticle-based plasmonics.[32,38–41] Research reports that the binding of $[Ru(bpy)_3]^{2+}$ to the metal surface results in quenching of its triplet excited state which has been attributed to energy or electron transfer processes. However, the influence of $[Ru(bpy)_3]^{2+}$ extends beyond direct energy or electron transfer processes. In particular, its adsorption on metal nanoparticles can induce controlled aggregation, thereby altering the electromagnetic and electronic environment of the nanoparticles. This aggregation-driven restructuring has implications for light–matter interactions and can significantly influence the dynamics of hot-carrier relaxation. Furthermore, elucidating charge transfer and energy transfer dynamics in such hybrid systems, particularly under conditions of aggregation is crucial for application of these hybrid systems in light harvesting and photocatalysis.[42,43]

The aggregation of gold nanoparticles introduces an additional degree of freedom that strongly modulates their optical response.[44,45] When nanoparticles form aggregates, the resulting nanogap-induced "hotspots" dramatically enhance electromagnetic fields, creating highly active plasmonic platforms.[46–48] These hotspots facilitate ultrasensitive detection and significantly enhance photochemical reactions.[15,48] Additionally, aggregation alters the collective electronic properties of the nanoparticle ensemble, changing the way energy is dissipated following photoexcitation.[47] Studies have shown that uncontrolled aggregation or instability of these hotspots can severely limit applications in catalysis and light harvesting.[49] In our previous publication, we have demonstrated controlled aggregation of Au nanospheres through adsorption of precise concentration of $[Ru(bpy)_3]^{2+}$ on the gold surface, which impacted the ground state properties of the plasmon band that enable changes to electronic properties of adsorbate molecules on the surfaces of gold nanoparticles with speeding up or slowing down of plasmon-molecule dynamics due to highly localized fields.[50] In the current study, we use the same procedure to facilitate aggregation of Au nanospheres and investigate the excited-state dynamics of these hybrid aggregates. X-ray absorption near-edge structure (XANES) spectroscopy and transient absorption (TA) spectroscopy are employed to probe the structural and ultrafast electronic changes induced by $[Ru(bpy)_3]^{2+}$ functionalization of 40 nm and 100 nm AuNPs.

X-ray techniques have often been employed to characterize nanoparticles.[51,52] XANES is highly sensitive to changes in the d-orbital configuration of Au atoms, and several studies have utilized the Au L_3 edge to study surface and size effects in systems such as gold nano clusters, colloidal gold, and gold nano wires, etc.[53–56] XANES can provide critical insight into changes in the electron distribution upon functionalization with the $[Ru(bpy)_3]^{2+}$ complex and subsequent aggregation.[57] Ultrafast spectroscopy, particularly TA spectroscopy, has proven to be a powerful tool for probing electron dynamics in metal nanoparticles enabling real-time monitoring of plasmon bleaching, energy dissipation, and relaxation pathways.[58–60] Understanding these mechanisms is crucial for creating systems with enhanced and tunable

properties for advancing plasmon-mediated chemistry in light-harvesting applications. Seminal work by El-Sayed and group have provided foundational insights into relaxation dynamics in gold nanoparticles.[19,47,59,61–64] They report that after excitation with an ultrafast pulse, the electrons thermalize via electron-electron (e-e) interaction. The "hot" electrons then equilibrate with the surrounding lattice via electron-phonon (e-ph) coupling. While these relaxation dynamics in gold nanoparticles have been well-studied by different groups, aggregation induced effects on these relaxation processes, especially in the presence of functional ligands like $[Ru(bpy)_3]^{2+}$ remains underexplored.[61,65–67] Moreover, these relaxation steps—often treated as sequential and independent—may in fact be strongly coupled under certain structural conditions, such as aggregation. This interplay between e-e scattering and e–ph coupling during the thermalization of hot carriers in aggregated systems has received limited attention. Understanding how aggregation affects the balance between these two pathways is essential for developing rational strategies to modulate energy dissipation in plasmonic materials.

This study addresses these issues by examining the structural and electronic effects of $[Ru(bpy)_3]^{2+}$ functionalization on citrate-capped AuNPs of 40 nm and 100 nm diameters, focusing on the effects of aggregation on the hot-carrier relaxation process. Using XANES, we demonstrate that $[Ru(bpy)_3]^{2+}$ binding induces aggregation without altering the oxidation state of gold. Aggregation effects are more pronounced in 40 nm nanoparticles, as evidenced by enhanced XANES signals and UV-Vis spectra. Transient absorption spectroscopy reveals faster electron-phonon relaxation in aggregated 40 nm AuNPs compared to isolated ones on account of larger phonon bath in the former. We also observe a concurrent suppression of e–e scattering—indicating a non-sequential, competitive interaction between these two processes. In contrast isolated and aggregated 100 nm nanoparticles exhibit minimal change in dynamics due to weaker aggregation.[50] Control experiments using salt-induced aggregation in the absence of $[Ru(bpy)_3]^{2+}$ confirm that aggregation, rather than specific chromophore–metal interactions, primarily governs the observed relaxation behavior. While

previous studies have explored the influence of aggregation on e–ph scattering rates, the simultaneous analysis of both e–ph and e–e relaxation dynamics through quantitative fitting of transient absorption data remains largely unexplored. This dual analysis provides a more complete picture of hot-carrier relaxation pathways and represents a unique contribution of the present work. Additionally, when comparing the 40 nm and 100 nm AuNPs, we observe relaxation dynamics governed by distinct size-dependent mechanisms. In 40 nm particles, stronger aggregation enhances interparticle coupling and increases the effective phonon bath volume, promoting more efficient energy transfer to the lattice. In contrast, 100 nm particles exhibit increased radiative and surface scattering, which reduces the extent of electronic heating and results in more subtle changes to relaxation behavior. By understanding and leveraging the coupled dynamics of e–e and e–ph scattering, this study offers a new framework for engineering nanoscale materials. These findings highlight the critical role of aggregation and functionalization in modulating plasmonic dynamics, providing insights for designing tailored plasmonic systems for sensing, catalysis, and energy conversion.

Methods

Sample Preparation and UV-Vis

Citrate-capped gold nanoparticles (AuNPs) with diameters of 40 nm and 100 nm were obtained from nanoComposix. Prior to sample preparation, the nanoparticles were sonicated at 25°C to ensure uniform dispersion, maintaining consistent room temperature conditions during preparation and transportation. *Tris*(bipyridine)-ruthenium(II) (Sigma Aldrich) molecules were added to the AuNP solution and vortexed to facilitate adsorption onto the surface of the AuNPs. $[Ru(bpy)_3]^{2+}$ solutions with concentrations of 2 μM and 10 μM were used for the 40 nm and 100 nm AuNPs, respectively, to achieve the desired oligomerization as demonstrated in our previous publication.[50]. This was followed by capping with 200 μL of polyvinylpyrrolidone (PVP) to prevent uncontrolled oligomerization. The prepared samples

were stored at ambient temperature in sealed, dark containers. For beamline analysis, the samples were transported to Brookhaven National Laboratory via ground transport. Five, 10 μL aliquots of the samples were sequentially drop-cast onto Norcada chips, with each layer allowed to dry for 15 minutes before the next addition. The prepared sample chips were then adhesively attached to standard aluminum mounting pins and loaded onto the sample stage for further analysis. For TA analysis, the prepared sample solution was placed in a 0.2 cm cuvette under nitrogen atmosphere. Specifically, we analyze four different samples in the current study - bare 40 nm AuNP (no $[Ru(bpy)_3]^{2+}$), 40 nm AuNP + $[Ru(bpy)_3]^{2+}$, bare 100 nm AuNP, and 100 nm AuNP + $[Ru(bpy)_3]^{2+}$.

A spectrophotometer in a double beam configuration (Cary 60, Agilent Technologies) was used to characterize the ground state absorption properties of the nanoparticle complexes dispersed in aqueous solution. Samples were purged with nitrogen in a 0.2 cm quartz cuvette, then sealed prior to measurements. The ground state absorption spectrum was monitored both before and after transient absorption to ensure particle melting or adsorbate molecule degradation was not occurring (Figure S1). All scans were solvent and baseline/zero corrected and a scanning range of 190 - 1100 nm was used.

XANES Experimental Setup

Data collection was performed at the 3-ID Hard X-ray Nanoprobe (HXN) beamline at the National Synchrotron Light Source-II (NSLS-II) facility, located at the Brookhaven National Laboratory. The detailed experimental setup has been described elsewhere.[68] Briefly, XRF data was collected using a nano-focused beam from a Freznel zone plate with an outer zone of 30 nm. A silicon drift detector positioned at 90° to the sample was used to collect the XRF spectrum while raster scanning the sample. Samples were kept under helium gas at a pressure of 250 mm Hg to maintain thermal stability and to reduce air scattering. Throughout the experiments, a photon flux exceeding 10^9 photons per second was maintained. A step size of 30 nm and an exposure time of 0.03 seconds per step were used for data acquisition.

Transient Absorption Experimental Setup

A Solstice Ace one-box regenerative amplifier was seeded by the output of a Spectra-Physics MaiTai Ti:Sapphire oscillator, which was pumped by a higher-energy Q-switched Ascend high-power laser. The regenerative amplifier output consisted of 800 nm pulses with a duration of 60 fs, a spectral full-width at half-maximum (FWHM) of 10-15 nm, repetition rate of 5kHz, and an average power of 7.5 W. A beam splitter was used to divide the amplifier output, directing 6.5 W into the TA setup of which 6 W was used to pump an optical parametric amplifier (TOPAS, Light Conversion) to generate the pump pulse at 454 nm. The remaining 0.5 W, after attenuation using ND filter, was used to generate the probe pulse via supercontinuum generation in a sapphire crystal. A four-pass delay stage in the probe line provided a temporal delay window of -5 ps to 200 ps. Parabolic mirrors were used to collimate and focus the white light probe into the sample, preventing dispersion of the broadband probe. An optical chopper in the pump line, operating at 2.5 kHz blocks every other pump pulse to enable shot-to-shot pump-ON vs pump-OFF data acquisition for active background subtraction. The pump was focused into the sample with an energy of 23 nJ per pulse and overlapped with the probe in the sample. After passing through the sample, the pump beam was dumped, while the probe beam was recorded using a line scan complementary metal-oxide semiconductor (CMOS) camera, which employed reference channel detection to correct for minor shot-to-shot fluctuations in pump power. The sample was continuously rastered to avoid accumulation of photoproducts in the pump-probe overlap region. The measurements were made at 54.7° (magic angle) relative polarization of pump and probe beams, which helps eliminate contributions from molecular reorientation or rotational diffusion. This ensures that the observed signal reflects only the intrinsic electronic or vibrational relaxation processes of the system. The instrument response function at 454 nm pump was determined to be 85 fs (Figure S2) using Perylene/cyclohexane solution. Each time delay was averaged for 3 s (15000 shots) and 4-5 individual TA scans were averaged depending on the signal strength to produce the average 2D TA data.

Data Acquisition and Processing

XANES data acquisition was performed using Bluesky user interface, a Python-based library developed at the NSLS-II facility.[69] Data visualization and analysis were carried out using XMIDAS, a specialized software program developed by the BNL staff, tailored for X-ray spectromicroscopy applications. XANES spectra were normalized to the intensity of the last data point in the energy spectrum. TA data acquisition was performed using Helios software provided by Ultrafast Systems. Each individual data set was pump scatter corrected, background subtracted, time zero corrected, and chirp corrected using Surface Xplorer (Ultrafast Systems) software. The data was was further analyzed to obtain transient spectra and kinetic data using Kimopack software.[70] The transient kinetic traces were globally fit using the Global Fit package in IGOR Pro. A custom function based on the kinetic model derived by the Sun group was implemented to simultaneously extract the electron–electron and electron–phonon relaxation times (see text for details on the model).[67] The model function was convolved with a Gaussian instrument response function to account for the finite temporal resolution of the experimental setup.

Results and Discussion

Structural and Electronic Modifications in Gold Nanoparticles Induced by $[Ru(bpy)_3]^{2+}$ Binding

Before delving into the detailed X-ray analysis, it is important to understand the structure and physical characteristics of the sample, as the gold L_3 edge is sensitive to bonding, the surrounding environment, and aggregation.[54,71] According to the literature, citrate-capped gold nanoparticles are surrounded by a citrate bi-layer approximately 10 nm thick, with free carboxylate groups extending outward.[72] These free carboxylate groups impart a negative charge to the gold nanospheres, stabilizing the gold solution through mutual electrostatic re-

pulsion. In the present study, the introduction of positively charged $[Ru(bpy)_3]^{2+}$ complexes neutralizes the negative surface charge on the gold nanoparticles, promoting their aggregation. Multiple $[Ru(bpy)_3]^{2+}$ molecules are adsorbed onto the citrate bi-layer surrounding the AuNS. Our previous study estimated the adsorption density to be approximately 960 molecules per nm^2 and 475 molecules per nm^2 for 40 nm and 100 nm gold nanosphere (AuNS), respectively where transmission electron microscopy (TEM) showed different aggregation states of the 40 nm and 100 nm metal-oligomers.[50]

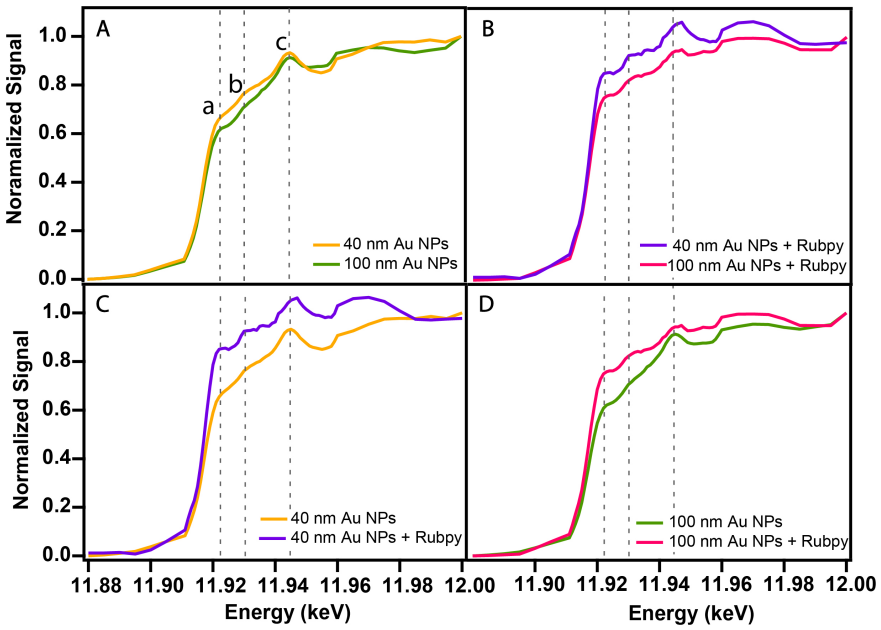

Figure 1: (A)-(D) Au L_3-XANES spectra for bare 40 nm AuNS (yellow), bare 100 nm AuNS (green), 40 nm AuNS + $[Ru(bpy)_3]^{2+}$ (purple), and 100 nm AuNS + $[Ru(bpy)_3]^{2+}$ (red). Lines a, b, and c correspond to peaks at 11.922 keV, 11.930 kev, and 11.945 keV, respectively.

Figure 1 presents the background-corrected and normalized XANES spectra obtained for the four AuNS samples described earlier. As shown in Figure 1A, the XANES spectra for the bare (unfunctionalized) 40 nm AuNS (yellow) and 100 nm AuNS (green) exhibit three distinct peaks at 11.922 keV, 11.930 keV, and 11.945 keV, labeled as a, b, and c, respectively. These observed peaks align with previously reported data for neutral gold species and are characteristic of transition metals with face-centered-cubic (fcc) structure.[73] Notably, no pre-edge features were observed, further confirming the absence of charged Au

species, as pre-edge features typically arise from core electron excitations into unoccupied orbitals.[56,71] Peak a, located at 11.922 keV and often referred to as the "white-line" peak, is commonly observed for transition metal elements.[54] This peak corresponds to the $2p_{3/2} \rightarrow 5d_{3/2}$ electronic transition, and its intensity reflects the number of 5d electron, thus indicating the oxidation state of the metal.[73] A pronounced white-line peak is generally indicative of a higher oxidation state. Bulk gold, with fully occupied d-orbitals, does not typically exhibit a white-line peak because the $2p_{3/2} \rightarrow 5d_{3/2}$ transition is not feasible. However, the weak white-line peak (a) observed in Figure 1 suggests a slightly oxidized state compared to bulk gold. This phenomenon can be attributed to a s-p-d type of hybridization. Specifically, hybridization between the $5d$ and $6s$ orbitals, resulting in the distribution of valence electrons into a electronic configuration of the type $5d^{10-\delta}6s^{1+\delta}$, which enables the $2p \rightarrow 5d$ transition.[51,74] Peak b, located at 11.930 keV, is relatively weak but has been consistently reported for bulk gold, gold nanowires and colloidal gold samples.[54]. Peak c, at 11.945 keV, is characteristic of bulk gold and provides insight into the local atomic structure surrounding the absorbing gold nanoparticle. Specifically, the intensity of peak c correlates with the number of neighboring atoms and general size of the metal nanostructure. A higher peak c intensity indicates an increased number of neighboring atoms, reflecting the structural arrangement. Previous X-ray studies on colloidal gold stabilized with sulfonated phosphine, with a particle diameter of 18 nm, reported structural and electronic properties similar to bulk gold.[54] Therefore, it is expected that the gold nanospheres in this study, with diameters 40 and 100 nm, will also exhibit behavior comparable to that of bulk gold given the spatial instrument resolution of the x-ray and optical setups which does not allow one to probe surface interactions alone.

Figure 1A displays similar spectral features for the 40 nm and 100 nm AuNS; however, the intensities of peak a and peak b are noticeably higher for 40 nm AuNS compared to 100 nm bare nanoparticles. As discussed earlier, the weak white-line peak observed in bulk gold arises from s-p-d hybridization, which redistributes a small amount of $5d$-character electrons into

the 6*s*-orbital, giving the metal center an "apparent" oxidation state higher than it actually is.[73] The slightly greater intensity of peaks *a* and *b* for the 40 nm particles can therefore be attributed either to more efficient s-p-d hybridization in the 40 nm AuNS compared to the 100 nm AuNS or to a potential charge transfer between the nanoparticle and the adsorbed molecules.[54] The electron-rich citrate layer on the gold surface, as demonstrated in prior studies, is not capable of oxidizing the gold nanoparticles.[72] Thus, the observed increase in intensity must primarily originate from more effective s-p-d hybridization in the 40 nm particles. This observation is inconsistent with prior observations, which suggest that hybridization efficiency decreases with nanoparticle size due to the reduction in the density of electronic states near Fermi level.[75,76] However, such size-dependent effects are typically observed only for nanoclusters or nanoparticles smaller than 5 nm. Since both the 40 nm and 100 nm samples exhibit bulk-like character, as noted earlier, these effects are unlikely to play a significant role.[76,77] Consequently, the increased intensity of peak *a* in the 40 nm AuNS relative to the 100 nm AuNS must arise primarily from the higher surface-to-volume ratio in the smaller nanoparticles. A moderate increase in the intensity of peak *c* is also observed for the 40 nm nanospheres compared to the 100 nm nanospheres; however, this enhancement is much less pronounced than that of peaks *a* and *b* (Figure 2, pink trace). This suggests minimal differences in the local atomic structure surrounding the 40 nm and 100 nm AuNS. Furthermore, no significant shift in the Au L_3 edge was observed between the two nanoparticle sizes.

As shown in Figure 1C and 1D, no significant shift is observed in the Au L_3 edge or the white-line peak (*a*) after functionalization with $[Ru(bpy)_3]^{2+}$ for both 40 nm and 100 nm AuNSs. A red or blue shift in the white-line peak energy would indicate a decrease or increase, respectively, in the oxidation state of the metal center. The absence of such a shift confirms that the oxidation state of gold remains unchanged before and after functionalization with $[Ru(bpy)_3]^{2+}$ complex. However, an increase in the overall XANES signal intensity is evident for both the 40 nm (Figures 2, green trace) and 100 nm (Figures 2, orange trace)

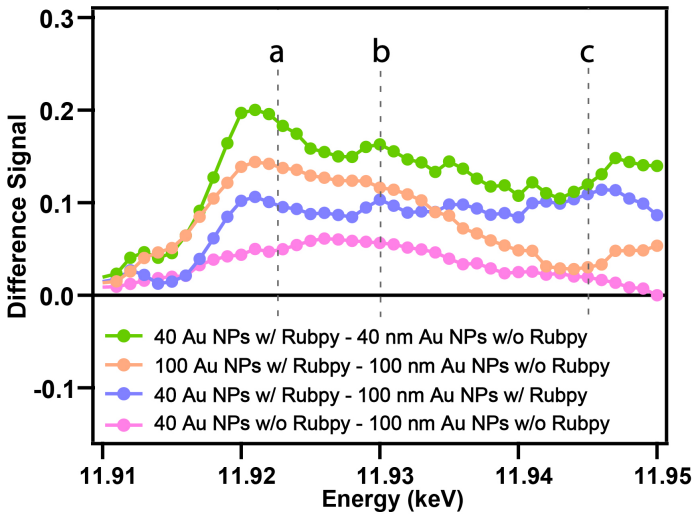

Figure 2: Difference between the XANES signals for bare and $[Ru(bpy)_3]^{2+}$ functionalized 40 nm and 100 nm Au nanospheres highlights the key difference between the spectra. Lines *a*, *b*, and *c* correspond to the difference XANES signal at 11.922 keV, 11.930 keV, and 11.945 keV respectively.

samples following $[Ru(bpy)_3]^{2+}$ binding. This increase can be attributed to possible charge transfer from the AuNS to $[Ru(bpy)_3]^{2+}$ complex, supported by a small shift in MLCT band of the fluorophore upon attachment to the AuNS, as demonstrated in previous studies.[50]. Furthermore, the observed increase in XANES signal intensity upon $[Ru(bpy)_3]^{2+}$ functionalization is more pronounced for the 40 nm AuNS compared to the 100 nm AuNS. As discussed earlier, 40 nm AuNS adsorb a greater number of $[Ru(bpy)_3]^{2+}$ complexes per nm^2 than 100 nm AuNS. Consequently, the stronger charge transfer effects in the 40 nm AuNS result in a more intense XANES signal. Additionally, it has been shown that when smaller gold nanoparticles aggregate, there is an increase in the density of states (DOS) near the Fermi level.[75]. This increase in DOS enhances the efficiency of s-p-d hybridization in gold, thereby amplifying the intensity of the white-light peak.[77] Thus, the aggregation of AuNS upon $[Ru(bpy)_3]^{2+}$ attachment likely contributes to the observed enhancement in the XANES signal (Figure 1C and 1D). Previous studies have also shown that the 100 nm AuNSs exhibit less extensive aggregation compared to the 40 nm AuNSs.[50] This observation further supports the smaller enhancement in XANES signal intensity for the 100 nm nanospheres

relative to the 40 nm nanospheres upon functionalization.

Peak *c* for the 100 nm sample exhibits a much smaller intensity increase compared to peaks *a* and *b*, as evident from the difference signal (Figure 2: orange trace) . Since the intensity of peak *c* corresponds to the number of neighboring atoms surrounding the absorbing atom, a smaller enhancement in peak *c* intensity suggests fewer neighboring atoms, indicative of reduced aggregation in the 100 nm sample.[78] Consistent with this observation, the XANES signal for the 40 nm + $[Ru(bpy)_3]^{2+}$ sample is more intense than that for the 100 nm + $[Ru(bpy)_3]^{2+}$ sample (see Figure 1B and Figure 2: purple trace). Moreover, the enhancement factor remains consistent across the entire XANES spectrum and is larger than the enhancement factor observed for the bare nanoparticles (Figure 2, pink trace). This increased enhancement can be attributed to the combined effects of charge transfer and aggregation, which are absent in the bare nanoparticles. These findings further support the conclusion from our previous study that 40 nm nanospheres exhibit better aggregation compared to 100 nm nanospheres. A closer examination of Figures 1C and 1D reveals a high-energy shift in peak *c* for both the 40 nm and 100 nm nanosphere upon functionalization with $[Ru(bpy)_3]^{2+}$. Consistent with previous XANES studies and corroborated by EXAFS (Extended X-Ray Absorption Fine Structure) for both gold and copper clusters, this shift indicates a decrease in the Au-Au (or Cu-Cu) distance.[55,78,79]. Although these earlier studies were conducted on gold nanoclusters, significantly smaller than the gold nanoparticles in the current study, the observed shifts can be rationalized in light of these findings. When two or more nanoparticles aggregate, the constituent atoms of the individual nanoparticles come close together, resulting in a reduction of the Au-Au distance and leading to a blue shift in peak *c*.

Size and Aggregation Effects on Plasmon Dynamics in Gold Nanoparticles

A clear understanding of the intrinsic excitation and relaxation behavior of citrate-stabilized Au nanospheres is crucial before disentangling the additional effects introduced by $[Ru(bpy)_3]^{2+}$ binding and subsequent aggregation. Figure 3 illustrates the evolution of the TA signal following the excitation of bare 40 nm AuNS with 454 nm pump. The most prominent feature is the ground-state bleach (GSB), also referred to as plasmon bleach, observed at 524 nm immediately after excitation. The GSB signal grows on the timescale of approximately 600 fs (Figure 3: Inset) and then recovers to a nearly constant value around 6 ps after the excitation pulse. Additionally, transient plasmon absorption (TPA) signals emerge on both the high-energy and low-energy sides of the GSB, centered at 489 nm and 565 nm, respectively. These TPA signals exhibit the same decay dynamics as the GSB described above. No significant changes in the spectral shape are observed for either signal throughout the measured delay times. The presence of two isosbestic points at 503 nm and 550 nm (Figure 3) suggests the existence of a common intermediate linking the GSB and TPA signals previously also observed in the picosecond dynamics of gold colloids, which indicate a redistribution of electrons that modify the transient dielectric function or the D(E, hω) density of states.[63,64]

According to the two-temperature model (TTM), the small electronic heat capacity relative to the lattice results in temperatures reaching of thousands of degrees immediately following excitation with an ultrashort pulse.[80] This leads to the creation of a non-Fermi electron distribution near the Fermi level. As described by Mie theory, plasmon bands arise from the oscillations of free conduction band electrons just above the Fermi level.[19,81] The excited non-Fermi electrons, however, do not oscillate at the same frequency as the unexcited electrons responsible for the plasmon band. Consequently, the excited electrons couple with the applied field at a different frequency, decreasing the intensity of the plasmon band at 524 nm. Additionally, the perturbed electron distribution near the Fermi level modifies the

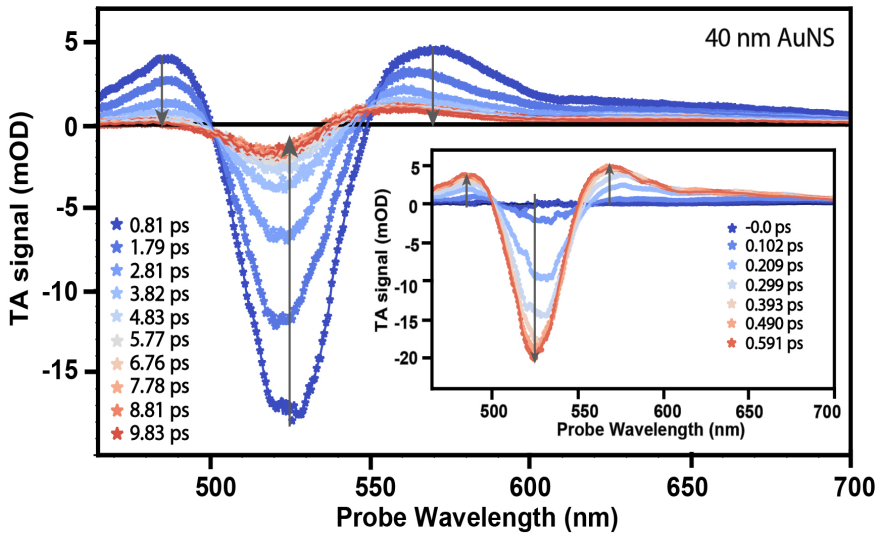

Figure 3: Evolution of the TA spectra of colloidal 40 nm Au nanosphere (no $[Ru(bpy)_3]^{2+}$) following excitation at 454 nm. Inset shows early time dynamics showing increase in the bleach signal in the first 700 fs.

real and imaginary dielectric constants, resulting in a broadening of the plasmon band.[65] This less intense and broad excited state signal manifests as "wings" on either side of the bleach (Figure 3). Therefore, the signal observed immediately after excitation represents the absorption spectrum of the excited state, rather than a true bleaching of ground state plasmon. Due to high electron density in gold, electron-electron (e-e) scattering occurs almost instantaneously, thermalizing the non-Fermi electron distribution on a femtosecond (fs) timescale and creating a "hot" electron distribution.[63,64] The initial increase in the bleach signal is attributed to this thermalization via e-e scattering, which increases the population of "hot" electrons. The bleach signal subsequently recovers as the electrons relax through electron-phonon (e-ph) and phonon-phonon (ph-ph) relaxation processes, occurring on short (1-3 ps) and longer ($>$ 50 ps) timescales, respectively.[64] Heat dissipation into the surrounding solvent alters its dielectric constant, which in turn shifts the plasmon resonance frequency. This shift is observed as a small blue shift in the bleach frequency (Figure 3: Inset).[82] Furthermore, we observe a narrowing of the plasmon bleach band which is attributed to cooling of the electron gas leading to lattice heating.[64] Similar spectral evolution traces were observed for other samples: 40 nm AuNS + $[Ru(bpy)_3]^{2+}$, 100 nm AuNS, and 100 nm AuNS

+ $[Ru(bpy)_3]^{2+}$ shown in Figures S5, S6, and S7, respectively. We observe that the bleach signal for the 100 nm samples is broader than that for the 40 nm samples, which can be attributed to the larger size of the 100 nm AuNS.[50 62] As the sphere diameter increases, scattering increasingly dominates the optical response, while for smaller diameters, absorption is the primary contributor. For example, in 100 nm gold spheres, the extinction cross-section comprises approximately 60% absorption and 40% scattering, whereas for smaller 40 nm gold spheres, absorption accounts for nearly 97% of the total extinction. Hence in 100 nm AuNS radiative damping becomes increasingly dominant. Unlike non-radiative damping, which typically results in faster dephasing and sharper resonance peaks, radiative damping contributes to broader, less intense LSPR bands due to energy loss via photon emission. Furthermore, phase retardation effects—arising from the spatial variation in the incident electric field across the larger particle—break the dipole approximation and activate higher-order multipolar plasmon modes. These combined effects lead to a noticeable broadening of the plasmon band in 100 nm AuNS under pulsed laser excitation.

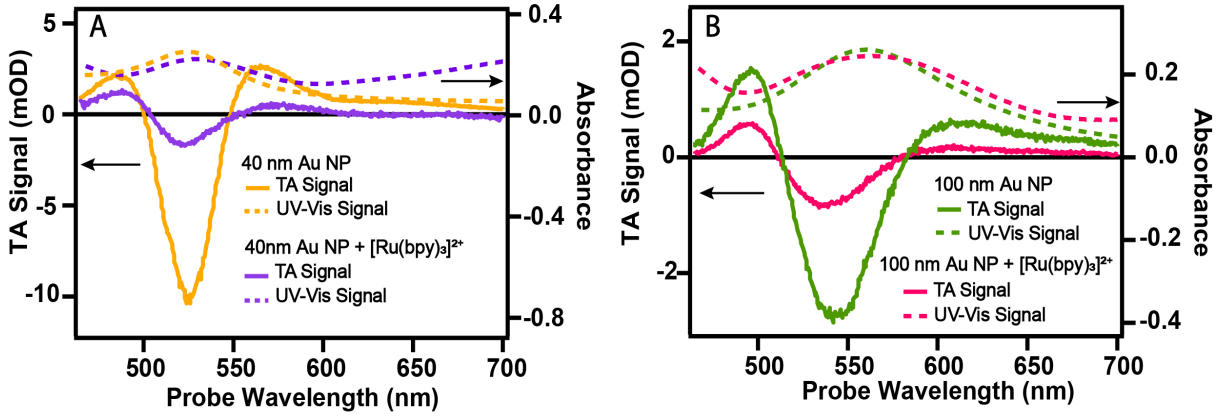

Figure 4: Transient absorption spectra for (A) colloidal 40 nm AuNS (yellow) and 100 nm AuNS (green) (B) 40 nm AuNS + $[Ru(bpy)_3]^{2+}$(purple) and 100 nm AuNS + $[Ru(bpy)_3]^{2+}$ (pink) samples measured at a delay of 1 ps following excitation at 454 nm pump. Ground state absorption for the respective samples, shown with dashed traces in corresponding colors as their TA spectra, are provided for comparison.

Figure 4A presents the TA spectral cuts for bare 40 nm AuNS (solid yellow trace) and $[Ru(bpy)_3]^{2+}$ functionalized 40 nm AuNS (solid purple trace) samples 1 ps after excitation.

For comparison, the ground state absorption spectra for both samples are also shown (dashed spectra). Figure 4B represents the same for 100 nm AuNS. Both the 40 nm and 100 nm samples exhibit monomer plasmon resonance bands in the 450 - 650 nm range, with the resonance band for the 100 nm nanospheres red shifted relative to the 40 nm nanosphere due to their larger size.[50] While the optical pump interacts with different points along the localized surface plasmon resonance (LSPR) scattering profile for 40 nm oligomers compared to 100 nm oligomers, previous studies have shown that the relaxation dynamics remain independent of the excitation pathway.[83] Additionally, as the size of the gold nanoparticles decreases, the influence of the LSPR diminishes.[84,85] Instead, a dominant interband pathway is favored following photon absorption, particularly at shorter (bluer) excitation wavelengths.[86] In both cases we observe that the LSPR band broadens and shifts to lower energies by about 4 nm upon binding with $[Ru(bpy)_3]^{2+}$ and subsequent aggregation. These observation are likely the result of interrelated effects - (1) adsorption of the complex modifies the local dielectric environment around the nanoparticles, increasing the effective refractive index, which can red-shift the LSPR. (2) electronic interactions at the metal–molecule interface may lead to partial charge transfer between the gold surface and the $[Ru(bpy)_3]^{2+}$ complex, altering the free electron density in the metal and thereby affecting the LSPR position. (3) chemical interface damping (CID) arising from strong electronic coupling between the nanoparticle and the adsorbed complex can introduce additional nonradiative decay pathways for the plasmon, leading to increased damping and spectral broadening.[87] Additionally, aggregation can also contribute to the observed red shift and broadening of the LSPR band due to plasmonic coupling between adjacent nanoparticles, multipolar mode formation, and changes in the local dielectric environment.[47] A secondary factor is the result of changes in instantaneous electronic temperature where a blue shift correlates to a decrease in electron temperatures on ultrafast timescales.[88] Specifically, the presence of adsorbate molecules acts to dissipate heat in the e-ph channel and subsequently into the lattice/solvent bath. Surface ligands directly impact mechanical coupling between the metal, dielectric or molecular layer, and surround-

ing solvent which influences the details of energy-dissipation in these complex materials.[89] These mechanisms are not mutually exclusive and are likely co-occurring, it is challenging to isolate the contribution of each to the overall spectral changes. Notably, in Figure 4B we observe that the plasmon bleach signal is blue-shifted compared to their corresponding ground state absorption (LSPR) band for both the bare ($\Delta\lambda$ = 16 nm) and $[Ru(bpy)_3]^{2+}$ functionalized ($\Delta\lambda$ = 24 nm) 100 nm particle. Similar observations were made for 40 nm sample (Figure 4A) but to a smaller degree, specifically the bleach signal for the bare and $[Ru(bpy)_3]^{2+}$ functionalized sample exhibiting blue shifts of 1 nm and 6 nm relative to the corresponding ground state LSPR band. It is important to note that high-intensity pump pulses (ranging from mJ/pulse to μJ/pulse) can generated significant heat in plasmonics samples, potentially leading to melting of the gold nanoparticles as reported in previous studies.[90] To mitigate this risk, the pump intensity in our current measurements was kept low (23 nJ/pulse), to obtain good signal-to-noise while avoiding overheating of the sample. Additionally, we performed pump power dependence study of the TA signal for the bare 40 nm sample, conforming that 23 nJ lies well within the linear excitation regime, where non-linear effects such as two-photon absorption are unlikely to occur (Figure S4). Therefore, the observed blue-shifts in the bleach signal are inherent to the sample dynamics and not artifacts of experimental conditions. Upon photoexcitation, the generation of a nonthermal electron distribution modifies the dielectric function, temporarily shifting the plasmon resonance to shorter wavelengths (blue shift). This effect is enhanced in functionalized and aggregated nanoparticles, where the local refractive index, chemical interface damping, and interparticle coupling perturb the LSPR. In our case, the blue shift is more pronounced in 100 nm particles despite their lower degree of aggregation compared to 40 nm ones, suggesting that the shift scales not just with aggregation but also with size-dependent radiative damping and retardation effects, which modulate the transient dielectric response more significantly in larger particles.

Figure 5 shows the normalized kinetic traces at transient bleach wavelengths of 524 nm

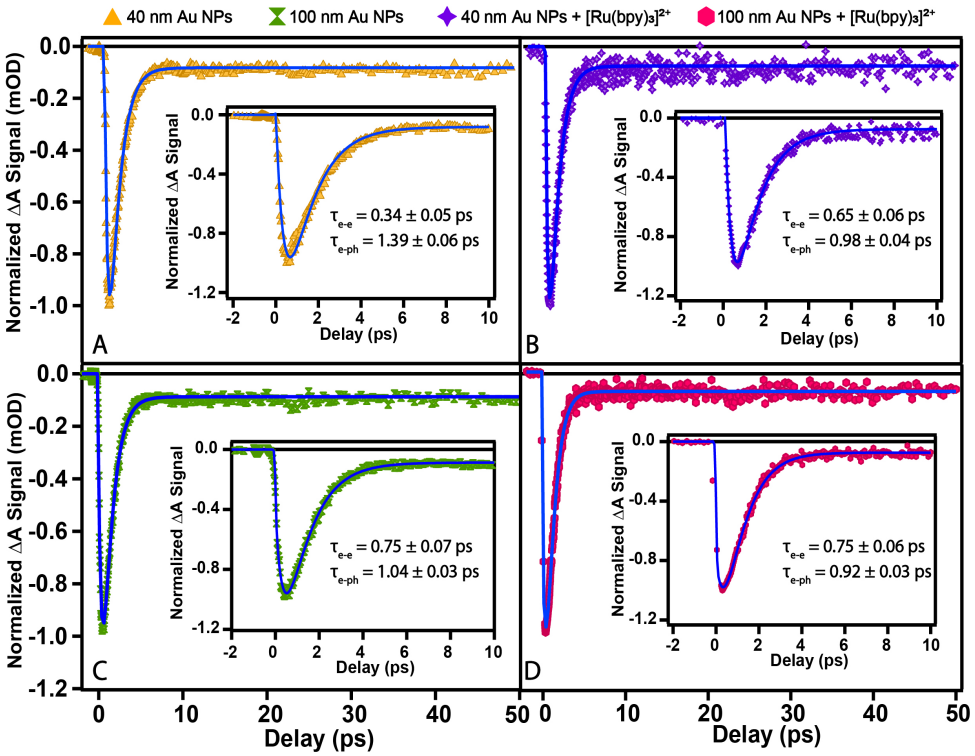

Figure 5: Normalized transient bleach dynamics for AuNS of different size and surface chemistry. Transient bleach kinetics are shown for (A) bare 40 nm AuNS (yellow), (B) 40 nm AuNS + $[Ru(bpy)_3]^{2+}$ (purple), (C) bare 100 nm AuNS (green), and (D) 100 nm AuNS + $[Ru(bpy)_3]^{2+}$ (red). The kinetic traces correspond probe wavelengths of 524 nm and 548 nm for 40 nm and 100 nm samples, respectively. Solid lines represent exponential fits based on equation 1. Insets within each subplots highlight the early-time plasmonic response upon excitation. Extracted decay constants are reported with 95% confidence interval.

and 548 nm, for the 40 nm and 100 nm samples, respectively. Qualitatively, the kinetic traces for the functionalized and unfunctionalized AuNS show no significant changes within the first 50 ps following excitation (Figure 5 A, B, C, and D). Generally, an increase in the transient bleach signal, caused by e-e scattering is observed creating a hot electron distribution with $T_e > T_0$, where T_e is the electron temperature after excitation and T_0 is the initial temperature of the system. The thermalized electron population then relaxes through e-ph scattering resulting in an increase in the lattice temperature as evidenced by the offset in the TA spectra. Ph-ph scattering occurs on much longer timescales ($\approx$ 200 ps), and the signal decays very slowly as the lattice equilibrates with the surrounding environment (Figure S9). To quantify the electron dynamics, the observed kinetics were modeled using

the rate equation derived by Sun. *et. al.*, where the induced change in transmission $\Delta T/T$ upon photo excitation is given as:

$$\frac{\Delta T}{T} = \left[1 - exp\left(\frac{-t}{\tau_{e-e}}\right)\right] exp\left(\frac{-t}{\tau_{e-ph}}\right) + \alpha \tag{1}$$

where, τ_{e-e} is the non-Fermi electron thermalization time (electron-electron scatter), τ_{e-ph} is the hot-electron decay time (electron-phonon scatter), and α accounts for heating of the lattice to a temperature higher than the initial temperature of the system upon electron-phonon coupling. The solid blue lines in Figure 5 represent global fits to the kinetic data used to determine τ_{e-e} and τ_{e-ph}. For bare 40 nm AuNS, the fit gave a rise time of 340 fs and a decay time of 1.4 ps for e-e and e-ph processes (Figure 5A), respectively, which is in agreement with previous measurements.[63] Upon $[Ru(bpy)_3]^{2+}$ functionalization and subsequent aggregation we observe an increase in the value of τ_{e-e} (650 fs) implying slowing down of the electron-electron scatter rate accompanied by a decrease in τ_{e-ph} (0.98 ps) value indicating a faster electron-phonon coupling. The faster relaxation dynamics observed in the 40 nm AuNS aggregates compared to isolated nanospheres can be attributed to enhanced e-ph coupling due to aggregation. The e-ph efficiency varies inversely with the electron oscillation frequency-phonon resonance detuning (EOPRD) (Equation 2).[47] EORPD determines the spectral overlap between the electron oscillation frequency and the phonon spectrum and is expressed as:

$$EORPD = \frac{v_f}{d} - \omega_d \tag{2}$$

where, v_f is the Fermi velocity of the Au electrons, ω_d is Au Debye frequency and d is the size of the area over which the hot electrons can be delocalized. Hence, increase in value of d upon aggregation results in decrease in electron oscillation frequency, and a subsequently decrease of EOPRD. This leads to increased e-ph scattering rates in aggregates compared to isolated AuNS. To understand the increase in e-e scatter time it is necessary to analyze

the mechanism of electron relaxation following ultrafast photoexcitation. Upon excitation with laser pulse a non-thermal (non-Fermi) electron distribution extending upto the pump photon energy ($h\nu$) is generated. This non-thermal population typically relaxes via e–e scattering, redistributing energy among the electronic subsystem and leading toward a hot electron distribution characterized by an elevated electronic temperature (T_e). This hot electron population then generally relaxes via e-ph scattering. However, it is important to note that the non-thermal electrons are not isolated from the lattice during this process. As the e-ph coupling becomes highly efficient in the case of aggregates, energy is transferred from the non-thermal electrons to the lattice before complete e–e thermalization is achieved. This energy loss reduces the difference between the actual non-thermal distribution and the equilibrium Fermi–Dirac distribution. Since the e–e scattering rate is directly proportional to this energy difference the decrease in energy content of the non-thermal electrons leads to a corresponding reduction in the e–e scattering rate.[19,66] Thus aggregation modifies the conventional sequential two-step relaxation mechanism and highlights the coupled dynamics of electron thermalization and lattice heating. To further support this mechanistic interpretation, we conducted additional control experiment where aggregation in 40 nm spheres was induced using aqueous NaCl, in the absence of the $[Ru(bpy)_3]^{2+}$ complex (Figure S10). This allowed us to isolate the effect of aggregation from that of molecular functionalization. Notably, the transient absorption data for these salt-induced aggregates revealed trends similar to those observed with $[Ru(bpy)_3]^{2+}$-functionalized nanoparticles. Specifically, we observed an enhancement in electron–phonon coupling—evidenced by shorter e–ph relaxation times—and a concomitant increase in electron–electron scattering times (Figure S10). These results reinforce our hypothesis that the observed changes in ultrafast dynamics are primarily driven by aggregation-mediated plasmonic coupling rather than chemical interactions with the chromophore.

Comparing figures 5C and 5D we observe only minor differences in the decay dynamics between the functionalized (green) and unfunctionalized (pink) 100 nm nanospheres. The e-e

scattering times are essentially identical at 0.75 ps for both samples, and the electron–phonon (e–ph) coupling times differ only slightly—1.04 ps for the unfunctionalized particles versus 0.92 ps for the functionalized ones. Although this modest increase in e–ph coupling is consistent with some degree of aggregation, the values lie well within the experimental uncertainty and do not suggest a strong deviation from the behavior of isolated nanospheres. This is consistent with the explanation above and previous findings, which indicate that 100 nm particles aggregate less than 40 nm particles.[50] Reduced aggregation in 100 nm particles results in weaker e-ph coupling and negligible changes in relaxation dynamics compared to isolated nanospheres (Equation 2).[47] Similar NaCl-induced aggregation experiments were also performed for the 100 nm AuNS. While the extent of aggregation remained lower compared to the 40 nm particles, we observed qualitatively similar trends—namely, a modest increase in e–ph coupling and a slight slowing of e–e scattering (Figure S11). A comparison between the 40 nm and 100 nm gold nanospheres reveals distinct differences in their ultrafast relaxation dynamics, both in the absence and presence of aggregation. In the non-aggregated state, the 40 nm particles exhibit a significantly shorter e–e scattering time (0.34 ps) compared to the 100 nm counterparts (0.75 ps), along with a slower e–ph coupling time of 1.39 ps versus 1.04 ps (Figure 5A and 5C). These trends can be rationalized by considering the size-dependent electron heating: for the same pump fluence, smaller nanoparticles reach higher electron temperatures due to their lower heat capacity and stronger absorption.[10,80] Elevated electron temperatures increase the rate of e–e scattering, but are known to reduce the e–ph coupling rate, leading to longer relaxation times.[80] This explains the faster e–e and slower e–ph times in 40 nm particles relative to 100 nm. For the aggregated 40 nm and 100 nm gold nanospheres, we observe a trend similar to isolated samples: the e–e scattering time is longer in 100 nm particle aggregates (0.75 ps) than in 40 nm particle aggregates (0.65 ps), while e–ph coupling is faster in the 100 nm aggregates (0.92 ps) compared to the 40 nm ones (0.98 ps). However, the extent of these differences is less pronounced than in the non-aggregated case. This is attributed to the fact that 100 nm particles undergo significantly

less aggregation than 40 nm particles, resulting in dynamics that remain largely similar to those of isolated particles. Thus while size dependent electron heating is preserved, its less prominent in the limited aggregates in 100 nm particles.

It should be noted that interband transition can occur at 454 nm, where the recombination of *d*-orbital hole with electrons above or below the Fermi level happens within tens of femtoseconds, well within the laser excitation window. While interband transitions may complicate the initial relaxation dynamics, they are unlikely to alter the overall relaxation picture significantly. We also note that the fluorescence intensity difference between Fig 1C and Fig 1D sheds light on understanding the differences in the decay lifetimes shown in Figure 5. There is greater electron-donating properties in the 40 nm nanocomposites due to stronger aggregation, therefore affecting the LSPR. Previously, we have shown that 40 nm and 100 nm gold nanoparticles have different absorption isotherms due to a saturation effect in the surface free energy of the 100 nm gold with different size-dependent molecular loading.[50] Our XANES suggests a disorder beyond a difference in adsorbate molecular coverage on the gold nanoparticle surface, which also impacts electronic structure. Following the introduction of the molecule to gold, there is a structural distortion in the gold lattice leading to greater electron donation to the Ru^{2+} and ligand assembly (Fig 1C and Fig 1D, peak c). This distortion then influences the aggregation dynamics and subsequently the degree of electron-phonon coupling followed by dissipation through these channels. Taken together, our XANES findings aid in elucidating the complex surface absorption dynamics in aggregated oligomers where an increase in peak c indicates atom-atom electronic reconfiguration that is more pronounced in the 40 nm than in the 100 nm. Furthermore, the $[Ru(bpy)_3]^{2+}$ adsorbate molecules significantly change this atom-atom electronic structure due to electrostatic interactions between the Ru^{2+} atoms and the negative citrate layer on the Au(0) surface. We correlate these changes in electronic structure to transient e-e scattering and e-ph pathways.

Conclusion

This study elucidates the role of molecular functionalization and controlled aggregation in modulating the ultrafast plasmonic dynamics of gold nanoparticles (AuNPs). Using X-ray absorption near-edge spectroscopy (XANES) and transient absorption (TA) spectroscopy, we investigated citrate-capped 40 nm and 100 nm AuNPs functionalized with $[Ru(bpy)_3]^{2+}$ to examine how nanoparticle size and aggregation state influence their electronic and energy dissipation behavior. XANES analysis revealed that $[Ru(bpy)_3]^{2+}$ functionalization induces controlled aggregation of gold nanoparticles without altering their oxidation state. The aggregation effects were more pronounced in 40 nm nanoparticles, as evidenced by enhanced XANES spectra. The enhancement in the white-line and post-edge features, particularly in the 40 nm particles, reflects increased s–p–d hybridization and a greater density of states near the Fermi level. These findings confirm the formation of aggregation-induced hotspots, which are critical for enhancing plasmonic coupling.

Transient absorption spectroscopy further demonstrated distinct differences in electron-phonon relaxation dynamics between 40 nm and 100 nm nanoparticles. Aggregated 40 nm nanoparticles exhibited faster e-ph relaxation dynamics relative to non-aggregated particles, due to increased effective area for electron delocalization and a correspondingly larger phonon bath upon aggregation. Concurrently, a slowing of electron–electron (e–e) scattering is observed in these aggregates, indicating that efficient energy transfer to the lattice occurs before full electronic thermalization is achieved. This interdependence of e–e and e–ph processes suggests a departure from the conventional sequential two-step relaxation model and points to coupled dynamics in aggregated systems. Conversely, 100 nm nanoparticles, which showed weaker aggregation, exhibited faster e-ph relaxation dynamics compared to aggregated 40 nm AuNS which we attribute to increased radiative and surface scattering. This leads to reduced optical absorption and lower electronic heating per unit volume, resulting in lower peak electron temperatures and consequently faster e-ph relaxation. The interplay between aggregation-induced coupling (40 nm AuNS) and scattering-mediated relaxation (100

nm AuNS) provides critical insights into the size-dependent energy dissipation pathways in functionalized plasmonic systems. The presence of isosbestic points in the TA spectra and shifts in the plasmon resonance frequency further highlight the complex dynamics at play in these hybrid systems.

These findings underscore the critical role of nanoparticle size and aggregation in modulating plasmonic dynamics and electron relaxation pathways. Although the $[Ru(bpy)_3]^{2+}$ complex plays a critical role in driving controlled nanoparticle aggregation, our comparative experiments with salt-induced aggregates demonstrate that the observed modulation of relaxation dynamics arises predominantly from the aggregation itself rather than specific chemical interactions with the chromophore. It further highlights how nanoscale assembly and coupling can redistribute energy dissipation pathways in a way that is highly dependent on both particle size and aggregate structure. Taken together, our findings demonstrate that aggregation is not merely an optical tuning mechanism but a critical factor in defining how plasmonic nanoparticles dissipate energy after excitation. This work not only advances our understanding of molecule-nanoparticle interactions but also offers pathways for optimizing these systems in applications such as sensing, catalysis, and light-energy conversion. Future studies should explore the effects of varying chromophore densities and molecular adsorbate properties to further unravel the complex interactions in plasmon-molecule hybrid systems. The integration of ultrafast spectroscopy with structural and computational techniques holds great promise for advancing the design of next-generation plasmonic materials.

Supporting Information

UV–vis absorption spectra of the samples, transient absorption data for perylene, X-ray fluorescence images, pump power dependence of transient absorption measurements, and additional transient absorption spectra.

Acknowledgment

This research used HXN-3ID of the National Synchrotron Light Source II, a U.S. Department of Energy (DOE) Office of Science User Facility operated for the DOE Office of Science by Brookhaven National Laboratory under Contract No. DE-SC0012704. The research in this paper was supported by EPSCoR Research Fellows National Science Foundation Grant (2429239) and Brown University's Initiative for Sustainable Energy Seed Grant (GR300322) and Brown University start-up funds.

References

(1) Liu, Z.; Xie, C.; Heumueller, T.; McCulloch, I.; Brabec, C. J.; Huang, F.; Cao, Y.; Li, N. A review on organic nanoparticle-based optoelectronic devices: from synthesis to applications. *Energy Environ. Sci.* **2025**, *18*, 155–193.

(2) Chen, H.-S.; Yang, P.; Khan, Z. H.; Wu, J. M.; Li, G.; Kamali, A. R. Quantum Dots and Nanoparticles in Light Emitting Diodes, Displays, and Optoelectronic Devices. *Journal of Nanomaterials* **2015**, *2015*, 371679.

(3) Montes-García, V.; Squillaci, M. A.; Diez-Castellnou, M.; Ong, Q. K.; Stellacci, F.; Samorì, P. Chemical sensing with Au and Ag nanoparticles. *Chem. Soc. Rev.* **2021**, *50*, 1269–1304.

(4) Kant, K. et al. Plasmonic nanoparticle sensors: current progress, challenges, and future prospects. *Nanoscale Horiz.* **2024**, *9*, 2085–2166.

(5) Yu, X.; Pu, H.; Sun, D.-W. Nano light conversion agents: recent advances, future prospects and challenges in enhancing plant green cultivation. *Journal of Cleaner Production* **2023**, *426*, 138919.

(6) Xu, X.; Shen, R.; Mo, L.; Yang, X.; Chen, X.; Wang, H.; Li, Y.; Hu, C.; Lei, B.;

Zhang, X.; et al. Improving Plant Photosynthesis through Light-Harvesting Upconversion Nanoparticles. *ACS Nano* **2022**, *16*, 18027–18037.

(7) Stefancu, A.; Halas, N. J.; Nordlander, P.; Cortes, E. Electronic excitations at the plasmon–molecule interface. *Nature Physics* **2024**, *20*, 1065–1077.

(8) Warren, N. L.; Yunusa, U.; Singhal, A. B.; Sprague-Klein, E. A. Facilitating excited-state plasmonics and photochemical reaction dynamics. *Chemical Physics Reviews* **2024**, *5*, 011307.

(9) Oh, H.; Searles, E. K.; Chatterjee, S.; Jia, Z.; Lee, S. A.; Link, S.; Landes, C. F. Plasmon Energy Transfer Driven by Electrochemical Tuning of Methylene Blue on Single Gold Nanorods. *ACS Nano* **2023**, *17*, 18280–18289.

(10) Hartland, G. V. Optical Studies of Dynamics in Noble Metal Nanostructures. *Chemical Reviews* **2011**, *111*, 3858–3887.

(11) Yaqoob, A. A.; Umar, K.; Ibrahim, M. N. M. Silver nanoparticles: various methods of synthesis, size affecting factors and their potential applications–a review. *Applied Nanoscience* **2020**, *10*, 1369–1378.

(12) Hammami, I.; Alabdallah, N. M.; jomaa, A. A.; kamoun, M. Gold nanoparticles: Synthesis properties and applications. *Journal of King Saud University - Science* **2021**, *33*, 101560.

(13) Mulvaney, P. Surface Plasmon Spectroscopy of Nanosized Metal Particles. *Langmuir* **1996**, *12*, 788–800.

(14) Langer, J. et al. Present and Future of Surface-Enhanced Raman Scattering. *ACS Nano* **2020**, *14*, 28–117.

(15) Brown, L. V.; Yang, X.; Zhao, K.; Zheng, B. Y.; Nordlander, P.; Halas, N. J. Fan-Shaped Gold Nanoantennas above Reflective Substrates for Surface-Enhanced Infrared Absorption (SEIRA). *Nano Letters* **2015**, *15*, 1272–1280.

(16) Badshah, M. A.; Koh, N. Y.; Zia, A. W.; Abbas, N.; Zahra, Z.; Saleem, M. W. Recent Developments in Plasmonic Nanostructures for Metal Enhanced Fluorescence-Based Biosensing. *Nanomaterials* **2020**, *10*, 1749.

(17) Hodak, J. H.; Henglein, A.; Hartland, G. V. Size dependent properties of Au particles: Coherent excitation and dephasing of acoustic vibrational modes. *The Journal of Chemical Physics* **1999**, *111*, 8613–8621.

(18) Jain, P. K.; Lee, K. S.; El-Sayed, I. H.; El-Sayed, M. A. Calculated Absorption and Scattering Properties of Gold Nanoparticles of Different Size, Shape, and Composition: Applications in Biological Imaging and Biomedicine. *The Journal of Physical Chemistry B* **2006**, *110*, 7238–7248.

(19) Link, S.; El-Sayed, M. A. Shape and size dependence of radiative, non-radiative and photothermal properties of gold nanocrystals. *International Reviews in Physical Chemistry* **2000**, *19*, 409–453.

(20) Yockell-Lelièvre, H.; Lussier, F.; Masson, J.-F. Influence of the Particle Shape and Density of Self-Assembled Gold Nanoparticle Sensors on LSPR and SERS. *The Journal of Physical Chemistry C* **2015**, *119*, 28577–28585.

(21) Naidu, G. N.; Kadria-Vili, Y.; Neumann, O.; Halas, N. J.; Nordlander, P.; Alabastri, A. Routes to Optimizing Photothermal Cancer Therapy through a Comprehensive Theoretical Model. *ACS Photonics* **2024**, *11*, 2681–2690.

(22) Yi, J.; You, E.-M.; Hu, R.; Wu, D.-Y.; Liu, G.-K.; Yang, Z.-L.; Zhang, H.; Gu, Y.; Wang, Y.-H.; Wang, X.; et al. Surface-enhanced Raman spectroscopy: a half-century historical perspective. *Chem. Soc. Rev.* **2025**, *54*, 1453–1551.

(23) Stefancu, A. et al. Impact of Surface Enhanced Raman Spectroscopy in Catalysis. *ACS Nano* **2024**, *18*, 29337–29379.

(24) Gawande, M. B.; Goswami, A.; Asefa, T.; Guo, H.; Biradar, A. V.; Peng, D.-L.; Zboril, R.; Varma, R. S. Core–shell nanoparticles: synthesis and applications in catalysis and electrocatalysis. *Chemical Society Reviews* **2015**, *44*, 7540–7590.

(25) An, K.; Somorjai, G. A. Size and Shape Control of Metal Nanoparticles for Reaction Selectivity in Catalysis. *ChemCatChem* **2012**, *4*, 1512–1524.

(26) Kang, G.; Hu, S.; Guo, C.; Arul, R.; Sibug-Torres, S. M.; Baumberg, J. J. Design rules for catalysis in single-particle plasmonic nanogap reactors with precisely aligned molecular monolayers. *Nature Communications* **2024**, *15*, 9220.

(27) Thomas, K. G.; Kamat, P. V. Chromophore-Functionalized Gold Nanoparticles. *Accounts of Chemical Research* **2003**, *36*, 888–898.

(28) Fan, J.; Cheng, Y.; Sun, M. Functionalized Gold Nanoparticles: Synthesis, Properties and Biomedical Applications. *The Chemical Record* **2020**, *20*, 1474–1504.

(29) Pramod, P.; Sudeep, P. K.; Thomas, K. G.; Kamat, P. V. Photochemistry of Ruthenium Trisbipyridine Functionalized on Gold Nanoparticles. *The Journal of Physical Chemistry B* **2006**, *110*, 20737–20741.

(30) Farcas, A.; Janosi, L.; Astilean, S. Size and surface coverage density are major factors in determining thiol modified gold nanoparticles characteristics. *Computational and Theoretical Chemistry* **2022**, *1209*, 113581.

(31) Lanquist, A. P.; Piechota, E. J.; Wickramasinghe, L. D.; Marques Silva, A.; Thummel, R. P.; Turro, C. New Tridentate Ligand Affords a Long-Lived 3MLCT Excited State in a Ru(II) Complex: DNA Photocleavage and 1O2 Production. *Inorganic Chemistry* **2023**, *62*, 15927–15935.

(32) Damrauer, N. H.; Boussie, T. R.; Devenney, M.; McCusker, J. K. Effects of Intraligand Electron Delocalization, Steric Tuning, and Excited-State Vibronic Coupling on the Photophysics of Aryl-Substituted Bipyridyl Complexes of Ru(II). *Journal of the American Chemical Society* **1997**, *119*, 8253–8268.

(33) Dongare, P.; Myron, B. D. B.; Wang, L.; Thompson, D. W.; Meyer, T. J. [Ru(bpy)3]2+ revisited. Is it localized or delocalized? How does it decay? *Coordination Chemistry Reviews* **2017**, *345*, 86–107.

(34) Han, G.; Li, G.; Huang, J.; Han, C.; Turro, C.; Sun, Y. Two-photon-absorbing ruthenium complexes enable near infrared light-driven photocatalysis. *Nature Communications* **2022**, *13*, 2288.

(35) Heinemann, F.; Karges, J.; Gasser, G. Critical Overview of the Use of Ru(II) Polypyridyl Complexes as Photosensitizers in One-Photon and Two-Photon Photodynamic Therapy. *Accounts of Chemical Research* **2017**, *50*, 2727–2736.

(36) Nastasi, F.; Santoro, A.; Serroni, S.; Campagna, S.; Kaveevivitchai, N.; Thummel, R. P. Early photophysical events of a ruthenium(II) molecular dyad capable of performing photochemical water oxidation and of its model compounds. *Photochemical & Photobiological Sciences* **2019**, *18*, 2164–2173.

(37) Sornambigai, M.; Bouffier, L.; Sojic, N.; Kumar, S. S. Tris(2,2'-bipyridyl)ruthenium (II) complex as a universal reagent for the fabrication of heterogeneous electrochemiluminescence platforms and its recent analytical applications. *Analytical and Bioanalytical Chemistry* **2023**, *415*, 5875–5898.

(38) Bhasikuttan, A. C.; Suzuki, M.; Nakashima, S.; Okada, T. Ultrafast Fluorescence Detection in Tris(2,2‘-bipyridine)ruthenium(II) Complex in Solution: Relaxation Dynamics Involving Higher Excited States. *Journal of the American Chemical Society* **2002**, *124*, 8398–8405.

(39) Motley, T. C.; Troian-Gautier, L.; Brennaman, M. K.; Meyer, G. J. Excited-State Decay Pathways of Tris(bidentate) Cyclometalated Ruthenium(II) Compounds. *Inorganic Chemistry* **2017**, *56*, 13579–13592.

(40) Kim, J.; Kang, D.-g.; Kim, S. K.; Joo, T. Role of coherent nuclear motion in the ultrafast intersystem crossing of ruthenium complexes. *Physical Chemistry Chemical Physics* **2020**, *22*, 25811–25818.

(41) Wallin, S.; Davidsson, J.; Modin, J.; Hammarström, L. Femtosecond Transient Absorption Anisotropy Study on [Ru(bpy)3]2+ and [Ru(bpy)(py)4]2+. Ultrafast Interligand Randomization of the MLCT State. *The Journal of Physical Chemistry A* **2005**, *109*, 4697–4704.

(42) Irgen-Gioro, S.; Yang, M.; Padgaonkar, S.; Chang, W. J.; Zhang, Z.; Nagasing, B.; Jiang, Y.; Weiss, E. A. Charge and energy transfer in the context of colloidal nanocrystals. *Chemical Physics Reviews* **2020**, *1*, 011305.

(43) Boerigter, C.; Aslam, U.; Linic, S. Mechanism of Charge Transfer from Plasmonic Nanostructures to Chemically Attached Materials. *ACS Nano* **2016**, *10*, 6108–6115.

(44) Halas, N. J.; Lal, S.; Chang, W.-S.; Link, S.; Nordlander, P. Plasmons in Strongly Coupled Metallic Nanostructures. *Chemical Reviews* **2011**, *111*, 3913–3961.

(45) Westcott, S. L.; Oldenburg, S. J.; Lee, T.; Halas, N. J. Construction of simple gold nanoparticle aggregates with controlled plasmon–plasmon interactions. *Chemical Physics Letters* **1999**, *300*, 651–655.

(46) Jain, P. K.; El-Sayed, M. A. Plasmonic coupling in noble metal nanostructures. *Chemical Physics Letters* **2010**, *487*, 153–164.

(47) Jain, P. K.; Qian, W.; El-Sayed, M. A. Ultrafast Electron Relaxation Dynamics in Cou-

pled Metal Nanoparticles in Aggregates. *The Journal of Physical Chemistry B* **2006**, *110*, 136–142.

(48) Chen, A.; DePrince III, A. E.; Demortière, A.; Joshi-Imre, A.; Shevchenko, E. V.; Gray, S. K.; Welp, U.; Vlasko-Vlasov, V. K. Self-Assembled Large Au Nanoparticle Arrays with Regular Hot Spots for SERS. *Small* **2011**, *7*, 2365–2371.

(49) Cortés, E.; Besteiro, L. V.; Alabastri, A.; Baldi, A.; Tagliabue, G.; Demetriadou, A.; Narang, P. Challenges in Plasmonic Catalysis. *ACS Nano* **2020**, *14*, 16202–16219.

(50) Yunusa, U.; Warren, N.; Schauer, D.; Srivastava, P.; Sprague-Klein, E. Plasmon resonance dynamics and enhancement effects in tris(2,2-bipyridine)ruthenium(ii) gold nanosphere oligomers. *Nanoscale* **2024**, *16*, 5601–5612.

(51) Giorgetti, M.; Aquilanti, G.; Ballarin, B.; Berrettoni, M.; Cassani, M. C.; Fazzini, S.; Nanni, D.; Tonelli, D. Speciation of Gold Nanoparticles by Ex Situ Extended X-ray Absorption Fine Structure and X-ray Absorption Near Edge Structure. *Analytical Chemistry* **2016**, *88*, 6873–6880.

(52) Mourdikoudis, S.; Pallares, R. M.; Thanh, N. T. K. Characterization techniques for nanoparticles: comparison and complementarity upon studying nanoparticle properties. *Nanoscale* **2018**, *10*, 12871–12934.

(53) Ohyama, J.; Teramura, K.; Shishido, T.; Hitomi, Y.; Kato, K.; Tanida, H.; Uruga, T.; Tanaka, T. In Situ Au L3 and L2 edge XANES spectral analysis during growth of thiol protected gold nanoparticles for the study on particle size dependent electronic properties. *Chemical Physics Letters* **2011**, *507*, 105–110.

(54) Benfield, R. E.; Grandjean, D.; Kröll, M.; Pugin, R.; Sawitowski, T.; Schmid, G. Structure and Bonding of Gold Metal Clusters, Colloids, and Nanowires Studied by EXAFS, XANES, and WAXS. *The Journal of Physical Chemistry B* **2001**, *105*, 1961–1970.

(55) López-Cartes, C.; Rojas, T. C.; Litrán, R.; Martínez-Martínez, D.; de la Fuente, J. M.; Penadés, S.; Fernández, A. Gold Nanoparticles with Different Capping Systems: An Electronic and Structural XAS Analysis. *The Journal of Physical Chemistry B* **2005**, *109*, 8761–8766.

(56) Henderson, G. S.; de Groot, F. M. F.; Moulton, B. J. A. X-ray Absorption Near-Edge Structure (XANES) Spectroscopy. *Reviews in Mineralogy and Geochemistry* **2014**, *78*, 75–138.

(57) Polte, J.; Kraehnert, R.; Radtke, M.; Reinholz, U.; Riesemeier, H.; Thünemann, A. F.; Emmerling, F. New insights of the nucleation and growth process of gold nanoparticles via in situ coupling of SAXS and XANES. *Journal of Physics: Conference Series* **2010**, *247*, 012051.

(58) Wang, Y.; Shi, H.; Shen, L.; Wang, Y.; Cronin, S. B.; Dawlaty, J. M. Ultrafast Dynamics of Hot Electrons in Nanostructures: Distinguishing the Influence on Interband and Plasmon Resonances. *ACS Photonics* **2019**, *6*, 2295–2302.

(59) Link, S.; El-Sayed, M. A. Optical Properties and Ultrafast Dynamics of Metallic Nanocrystals. *Annual Review of Physical Chemistry* **2003**, *54*, 331–366.

(60) Liu, Y.; Chen, Q.; Cullen, D. A.; Xie, Z.; Lian, T. Efficient Hot Electron Transfer from Small Au Nanoparticles. *Nano Letters* **2020**, *20*, 4322–4329.

(61) Link, S.; Burda, C.; Mohamed, M. B.; Nikoobakht, B.; El-Sayed, M. A. Femtosecond transient-absorption dynamics of colloidal gold nanorods: Shape independence of the electron-phonon relaxation time. *Physical Review B* **2000**, *61*, 6086–6090.

(62) Link, S.; El-Sayed, M. A. Spectral Properties and Relaxation Dynamics of Surface Plasmon Electronic Oscillations in Gold and Silver Nanodots and Nanorods. *The Journal of Physical Chemistry B* **1999**, *103*, 8410–8426.

(63) Ahmadi, T. S.; Logunov, S. L.; El-Sayed, M. A. Picosecond Dynamics of Colloidal Gold Nanoparticles. *The Journal of Physical Chemistry* **1996**, *100*, 8053–8056.

(64) Logunov, S. L.; Ahmadi, T. S.; El-Sayed, M. A.; Khoury, J. T.; Whetten, R. L. Electron Dynamics of Passivated Gold Nanocrystals Probed by Subpicosecond Transient Absorption Spectroscopy. *The Journal of Physical Chemistry B* **1997**, *101*, 3713–3719.

(65) Hodak, J.; Martini, I.; Hartland, G. V. Ultrafast study of electron–phonon coupling in colloidal gold particles. *Chemical Physics Letters* **1998**, *284*, 135–141.

(66) Sun, C.-K.; Vallée, F.; Acioli, L.; Ippen, E. P.; Fujimoto, J. G. Femtosecond investigation of electron thermalization in gold. *Physical Review B* **1993**, *48*, 12365–12368.

(67) Sun, C.-K.; Vallée, F.; Acioli, L. H.; Ippen, E. P.; Fujimoto, J. G. Femtosecond-tunable measurement of electron thermalization in gold. *Physical Review B* **1994**, *50*, 15337–15348.

(68) Pattammattel, A.; Tappero, R.; Ge, M.; Chu, Y. S.; Huang, X.; Gao, Y.; Yan, H. High-sensitivity nanoscale chemical imaging with hard x-ray nano-XANES. *Science Advances* **2020**, *6*, eabb3615.

(69) Pattammattel, A.; Tappero, R.; Gavrilov, D.; Zhang, H.; Aronstein, P.; Forman, H. J.; O'Day, P. A.; Yan, H.; Chu, Y. S. Multimodal X-ray nano-spectromicroscopy analysis of chemically heterogeneous systems. *Metallomics* **2022**, *14*, mfac078.

(70) Müller, C.; Pascher, T.; Eriksson, A.; Chabera, P.; Uhlig, J. KiMoPack: A python Package for Kinetic Modeling of the Chemical Mechanism. *The Journal of Physical Chemistry A* **2022**, *126*, 4087–4099.

(71) Iglesias-Juez, A.; Chiarello, G. L.; Patience, G. S.; Guerrero-Pérez, M. O. Experimental methods in chemical engineering: X-ray absorption spectroscopy—XAS, XANES, EXAFS. *The Canadian Journal of Chemical Engineering* **2022**, *100*, 3–22.

(72) Park, J.-W.; Shumaker-Parry, J. S. Structural Study of Citrate Layers on Gold Nanoparticles: Role of Intermolecular Interactions in Stabilizing Nanoparticles. *Journal of the American Chemical Society* **2014**, *136*, 1907–1921.

(73) Coulthard, I.; Degen, S.; Zhu, Y. J.; Sham, T. K. Gold nanoclusters reductively deposited on porous silicon: morphology and electronic structures. *Canadian Journal of Chemistry* **1998**, *76*, 1707–1716.

(74) Pantelouris, A.; Kueper, G.; Hormes, J.; Feldmann, C.; Jansen, M. Anionic Gold in Cs3AuO and Rb3AuO Established by X-ray Absorption Spectroscopy. *Journal of the American Chemical Society* **1995**, *117*, 11749–11753.

(75) Liu, H.; Mun, B. S.; Thornton, G.; Isaacs, S. R.; Shon, Y.-S.; Ogletree, D. F.; Salmeron, M. Electronic structure of ensembles of gold nanoparticles: Size and proximity effects. *Physical Review B* **2005**, *72*, 155430.

(76) van Bokhoven, J. A.; Miller, J. T. d Electron Density and Reactivity of the d Band as a Function of Particle Size in Supported Gold Catalysts. *The Journal of Physical Chemistry C* **2007**, *111*, 9245–9249.

(77) Lei, Y.; Jelic, J.; Nitsche, L. C.; Meyer, R.; Miller, J. Effect of Particle Size and Adsorbates on the L3, L2 and L1 X-ray Absorption Near Edge Structure of Supported Pt Nanoparticles. *Topics in Catalysis* **2011**, *54*, 334–348.

(78) Greaves, G. N.; Durham, P. J.; Diakun, G.; Quinn, P. Near-edge X-ray absorption spectra for metallic Cu and Mn. *Nature* **1981**, *294*, 139–142.

(79) D. Bazin, V. B. P. S., A. Bensaddik Multiple Scattering Calculation of Absorption Spectrum and Diffraction Calculation: Application to Nanometer Scale Copper Metallic Particle. *J. Phys. IV France* **1996**, *6*, 481–485.

(80) Voisin, C.; Del Fatti, N.; Christofilos, D.; Vallée, F. Ultrafast Electron Dynamics and Optical Nonlinearities in Metal Nanoparticles. *The Journal of Physical Chemistry B* **2001**, *105*, 2264–2280.

(81) Tcherniak, A.; Ha, J. W.; Dominguez-Medina, S.; Slaughter, L. S.; Link, S. Probing a Century Old Prediction One Plasmonic Particle at a Time. *Nano Letters* **2010**, *10*, 1398–1404.

(82) Kamat, P. V. Photophysical, Photochemical and Photocatalytic Aspects of Metal Nanoparticles. *The Journal of Physical Chemistry B* **2002**, *106*, 7729–7744.

(83) Chiang, W.-Y.; Bruncz, A.; Ostovar, B.; Searles, E. K.; Brasel, S.; Hartland, G.; Link, S. Electron–Phonon Relaxation Dynamics of Hot Electrons in Gold Nanoparticles Are Independent of Excitation Pathway. *The Journal of Physical Chemistry C* **2023**, *127*, 21176–21185.

(84) Wu, Y.; Yang, M.; Ueltschi, T. W.; Mosquera, M. A.; Chen, Z.; Schatz, G. C.; Van Duyne, R. P. SERS Study of the Mechanism of Plasmon-Driven Hot Electron Transfer between Gold Nanoparticles and PCBM. *The Journal of Physical Chemistry C* **2019**, *123*, 29908–29915.

(85) Giri, S. K.; Schatz, G. C. Photodissociation of H2 on Ag and Au Nanoparticles: Effect of Size and Plasmon versus Interband Transitions on Threshold Intensities for Dissociation. *The Journal of Physical Chemistry C* **2023**, *127*, 4115–4123.

(86) Chiang, W.-Y.; Bruncz, A.; Ostovar, B.; Searles, E. K.; Brasel, S.; Hartland, G.; Link, S. Electron–Phonon Relaxation Dynamics of Hot Electrons in Gold Nanoparticles Are Independent of Excitation Pathway. *The Journal of Physical Chemistry C* **2023**, *127*, 21176–21185.

(87) Foerster, B.; Joplin, A.; Kaefer, K.; Celiksoy, S.; Link, S.; Sönnichsen, C. Chemical

Interface Damping Depends on Electrons Reaching the Surface. *ACS Nano* **2017**, *11*, 2886–2893.

(88) Bykov, A. Y.; Xie, Y.; Krasavin, A. V.; Zayats, A. V. Broadband Transient Response and Wavelength-Tunable Photoacoustics in Plasmonic Hetero-nanoparticles. *Nano Letters* **2023**, *23*, 2786–2791.

(89) Cheng, Y.; Smith, K. J.; Arinze, E. S.; Dziatko, R. A.; Gao, T.; Frank, B. P.; Thon, S. M.; Bragg, A. E. Size- and Surface-Dependent Photoresponses of Solution-Processed Aluminum Nanoparticles. *ACS Photonics* **2020**, *7*, 637–645.

(90) Link, S.; Burda, C.; Nikoobakht, B.; El-Sayed, M. A. Laser-Induced Shape Changes of Colloidal Gold Nanorods Using Femtosecond and Nanosecond Laser Pulses. *The Journal of Physical Chemistry B* **2000**, *104*, 6152–6163.

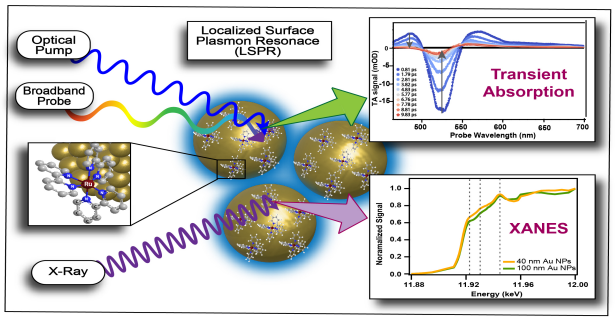

TOC Graphic